




## Article

# Novel Silica Hybrid Xerogels Prepared by Co-Condensation of TEOS and ClPhTEOS: A Chemical and Morphological Study

Guillermo Cruz-Quesada <sup>1</sup>, Maialen Espinal-Viguri <sup>1,\*</sup>, María Victoria López-Ramón <sup>2</sup>  
and Julián J. Garrido <sup>1,\*</sup>

<sup>1</sup> Institute for Advanced Materials and Mathematics (INAMAT2), Department of Science, Public University of Navarre (UPNA), Campus Arrosadia, 31006 Pamplona, Spain

<sup>2</sup> Department of Inorganic and Organic Chemistry, Faculty of Experimental Sciences, University of Jaen, 23071 Jaen, Spain

\* Correspondence: maialen.espinal@unavarra.es (M.E.-V.); j.garrido@unavarra.es (J.J.G.); Tel.: +34-948-169604 (M.E.-V.); +34-948-169601 (J.J.G.)

**Abstract:** The search for new materials with improved properties for advanced applications is, nowadays, one of the most relevant and booming fields for scientists due to the environmental and technological needs of our society. Within this demand, hybrid siliceous materials, made out of organic and inorganic species (ORMOSILs), have emerged as an alternative with endless chemical and textural possibilities by incorporating in their structure the properties of inorganic compounds (i.e., mechanical, thermal, and structural stability) in synergy with those of organic compounds (functionality and flexibility), and thus, bestowing the material with unique properties, which allow access to multiple applications. In this work, synthesis using the sol-gel method of a series of new hybrid materials prepared by the co-condensation of tetraethoxysilane (TEOS) and 4-chlorophenyltriethoxysilane (ClPhTEOS) in different molar ratios is described. The aim of the study is not only the preparation of new materials but also their characterization by means of different techniques (FT-IR, <sup>29</sup>Si NMR, X-ray Diffraction, and N<sub>2</sub>/CO<sub>2</sub> adsorption, among others) to obtain information on their chemical behavior and porous structure. Understanding how the chemical and textural properties of these materials are modulated with respect to the molar percentage of organic precursor will help to envisage their possible applications: From the most conventional such as catalysis, adsorption, or separation, to the most advanced in nanotechnology such as microelectronics, photoluminescence, non-linear optics, or sensorics.

**Keywords:** xerogels; hybrid materials; TEOS; chlorophenyltriethoxysilane; chemical-textural properties; ORMOSILs; ordered structures; silica species



**Citation:** Cruz-Quesada, G.; Espinal-Viguri, M.; López-Ramón, M.V.; Garrido, J.J. Novel Silica Hybrid Xerogels Prepared by Co-Condensation of TEOS and ClPhTEOS: A Chemical and Morphological Study. *Gels* **2022**, *8*, 677. <https://doi.org/10.3390/gels8100677>

Academic Editors: Zoltán Dudás and Adél Len

Received: 29 September 2022

Accepted: 17 October 2022

Published: 20 October 2022

**Publisher's Note:** MDPI stays neutral with regard to jurisdictional claims in published maps and institutional affiliations.



**Copyright:** © 2022 by the authors. Licensee MDPI, Basel, Switzerland. This article is an open access article distributed under the terms and conditions of the Creative Commons Attribution (CC BY) license (<https://creativecommons.org/licenses/by/4.0/>).

## 1. Introduction

Silica hybrid gels are among the so-called organic modified silica (ORMOSILs). Nowadays, these materials are being used for multiple applications such as the adsorption of metals in water [1–3], catalyst support [4–6], support for luminescent compounds [7–9], anti-corrosive or fungicide coatings [10–13], and biomedicine [14–19]. The key behind the tunability of the properties of these materials is the synergetic effect that generates the coexistence, at a nanometric scale, of an inorganic skeleton with flexible and functional organic constituents [20,21]. The hybrid gels are prepared by the sol-gel method, a very versatile synthetic technique that allows different approaches: (i) Anchoring of organic molecules in the porous of the already-formed solid gel [1,2,7–9], (ii) grafting of organic moieties on the surface of a silica material [4,22,23], (iii) co-condensation of an organosilane (SiR<sub>x</sub>(OR')<sub>4-x</sub>), with a carbon precursor, to form Si-O-C xerogels [16,18,24,25], or finally, (iv) classic co-condensation of a tetraalkoxysilane (Si(OR)<sub>4</sub>), usually tetraethoxysilane (TEOS), with one or more organosilanes [8–10]. In the latter approach, to obtain materials with the desired properties, it is of paramount importance to control the precursors' hydrolysis

and condensation reactions (Figure 1), due to their susceptibility to the media conditions (pH, solvents, use or not of a catalyst, proportions of H<sub>2</sub>O/precursor or organosilane/tetraalkoxysilane) [26–30].

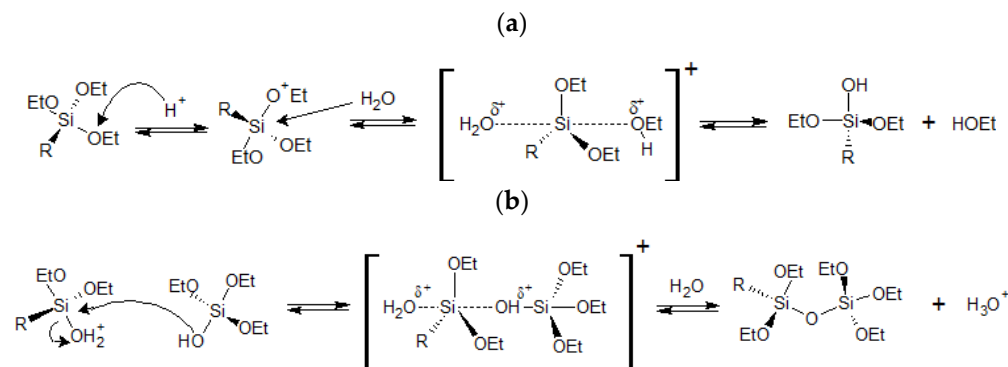


**Figure 1.** Mechanism in acidic media of (a) the first hydrolysis reaction of tetraethoxysilane (R = OEt) or triethoxysilane (R = alkyl or aryl), and (b) the co-condensation reaction of tetraethoxysilane with a triethoxysilane (R = alkyl or aryl).

The influence of these parameters in the synthesis of silica xerogels has been studied by our research group in recent years [31–34], with special emphasis on the nature and molar proportion of organosilanes in hybrid xerogels [35–37]. By means of different techniques, such as mass spectroscopy, inelastic neutron scattering, and infrared spectra deconvolution, it was confirmed that ordered domains of polyhedral oligomeric silsesquioxanes (POSS) are formed within the silica matrix of the hybrid materials, due to the blocking of the condensation direction in the organic precursor RTEOS (RTEOS = alkyl/chloroalkyl triethoxysilanes) and the intermolecular forces (e.g., hydrophobic or electrostatic interactions) exerted by the organic moieties [38–40]. In fact, ordered domains were detected at lower molar percentages of organic precursor when chloroalkyltriethoxysilanes (CIRTEOS) are used instead of their analogous alkoxysilanes [37,40]. The knowledge acquired in those studies has been used to prepare optical fiber sensors (OFS) by dip-coating, using selected gels with specific properties. These sensors have a labile and specific interaction with different adsorbates, such as vapor of water and volatile organic compounds (COVs), allowing their detection and monitoring [41–43].

Following this line of research, the aim of the present work is to study the morphological, textural, and chemical properties of silica hybrid xerogels containing a chlorophenyl moiety, and to evaluate their use as coatings for OFS in the future. For this purpose, a new series of transparent hybrid xerogels were prepared by co-condensation, in acidic media, of TEOS with (*p*-chlorophenyl) triethoxysilane (ClPhTEOS) at different molar percentages. The resulting materials were fully characterized by <sup>29</sup>Si NMR (Nuclear Magnetic Resonance), XRD (X-ray Diffraction), FTIR (Fourier-Transform Infrared Spectroscopy), Helium Pycnometry, FE-SEM (Field-Emission Scanning Electron Microscopy), HR-TEM (High-Resolution Transmission Spectroscopy), and the adsorption of N<sub>2</sub> (−196 °C) and CO<sub>2</sub> (0 °C). In addition, a modified and adjusted deconvolution method of the FT-IR spectra was used to acquire semi-quantitative information about the proportion of (SiO)<sub>4</sub> and (SiO)<sub>6</sub> rings [40,44], which are related to ordered structures and amorphous silica, respectively. Finally, the results were compared with those of the previously studied xerogels to remark on the influence of the chlorophenyl moiety on the material’s properties.

## 2. Results and Discussion

### 2.1. FT-IR

Figure 2 depicts the FT-IR spectra in the range of 1600–400 cm<sup>−1</sup> of the hybrid xerogels synthesized at different molar percentages of organic precursor. The spectra in the range of 4000–2750 cm<sup>−1</sup> are displayed in Figure S1 of the Supplementary Material.

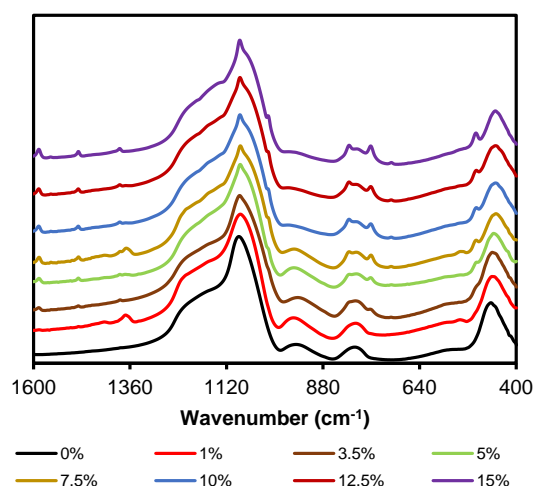


**Figure 2.** FT-IR spectra (range 1600–400  $\text{cm}^{-1}$ ) of the reference (100%TEOS) and the hybrid materials at different molar percentages of organic precursor (CIPhTEOS).

In Figure 2, the characteristic bands of the amorphous silica matrix can be observed: (i) Rocking of O–Si–O at  $455 \text{ cm}^{-1}$  ( $\rho$  O–Si–O), (ii) symmetric Si–O–Si stretching vibration at  $800 \text{ cm}^{-1}$  ( $\nu_s$  Si–O–Si), (iii) Si–O bond stretching vibration of the silanols on the surface at  $955 \text{ cm}^{-1}$  ( $\nu_s$  Si–OH), (iv) asymmetric Si–O–Si stretching vibration at  $1090 \text{ cm}^{-1}$  ( $\nu_{as}$  Si–O–Si), and (v) a wide and intense shoulder from 1350 to  $1120 \text{ cm}^{-1}$  associated with various vibrational modes of the Si–O–Si [45]. Additionally, a slight shoulder at  $550 \text{ cm}^{-1}$  can be observed, which is associated with the presence of 4-member siloxane rings,  $(\text{SiO})_4$  [46]. In the spectra, as the molar percentage of organic precursor gradually increases, a new incipient shoulder becomes more evident at 1140 and  $1155 \text{ cm}^{-1}$ , and the band at  $1080 \text{ cm}^{-1}$  narrows and stands out, similar to an emerging peak. These changes could indicate that the organic precursor is favoring the formation, within the silica matrix, of new structures with vibration modes ( $\nu_{as}$  Si–O–Si) at different specific frequencies [40]. In the spectral region of  $400\text{--}2750 \text{ cm}^{-1}$  (Figure S1 of the Supplementary Material), it is possible to observe the stretching bands of superficial silanols ( $\nu$  Si–OH a  $3450 \text{ cm}^{-1}$ ) and those resulting from the interaction of these groups through hydrogen bonds ( $\nu$  Si–OH–H at  $3660 \text{ cm}^{-1}$ ) [45].

The presence of the chlorophenyl moiety in the hybrid materials can be confirmed by a set of bands observed in the spectra: (i) The stretching bands of the hydrogens of the benzene ring in the range of  $3090\text{--}3010 \text{ cm}^{-1}$  ( $\nu$  (C–H), Figure S1), (ii) three C=C bond stretching bands in the spectral range of  $1450\text{--}1000 \text{ cm}^{-1}$  ( $1380$ ,  $1085$  and  $1015 \text{ cm}^{-1}$ ), and finally, (iii) three bands corresponding to the deformation vibrations of the C–H bonds in the aromatic rings (at  $815$ ,  $760$ , and  $500 \text{ cm}^{-1}$ ), and a band due to the stretching vibration of the C–Cl bond (at  $710 \text{ cm}^{-1}$ ) [43,47,48]. It should be noted that the spectrum of the xerogel 20CIPh is not shown in Figure 2 because a heterogeneous monolith with two well-differentiated phases was obtained: A non-colored transparent phase above (monolith) and an opaque phase below (precipitate), whose spectra turned out to be very different (Figure S2c in the Supplementary Material). This difference might be because the organic precursor favors the formation of structures with lower solubility in the reaction media, and thus precipitates. To test this hypothesis and obtain information on those structures, a material using only CIPhTEOS was synthesized, resulting in a white, soft, and extremely hydrophobic solid (100CIPh) (Figure S2d in the Supplementary Material). Figure 3 depicts the FT-IR spectra of the reference, 15CIPh, 20CIPh (monolith and precipitate), and 100CIPh, while Table 1 displays the list of bands observed in the spectrum of 100CIPh, the vibrations and structures assigned to those bands, and the literature consulted for the assignment.

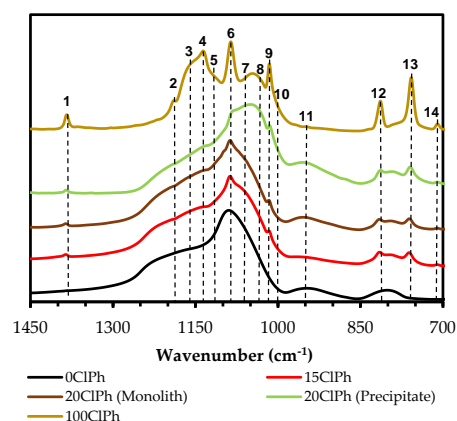


**Figure 3.** FT-IR spectra (range 1400–900  $\text{cm}^{-1}$ ) of the reference, 15ClPh, and both phases of 20ClPh and 100ClPh.

**Table 1.** List of FT-IR bands of the 100ClPh spectrum and proposed assignation based on the literature.

N°	Wavelength	Vibration	Structural	Reference
	( $\text{cm}^{-1}$ )	Assignment	Unit	
1	1380	$\nu$ (C=C)	Si-Ph-Cl	[36,48]
2	1190	$\nu_{\text{as}}$ (Si-O-Si), LO mode	(SiO) <sub>6</sub>	[40,44]
3	1160	$\nu_{\text{ring-as}}$ (Si-O-Si), LO mode	(SiO) <sub>4</sub> ; T <sub>7</sub>	[49]
4	1135	$\nu_{\text{ring-as}}$ (Si-O-Si), LO mode	(SiO) <sub>4</sub> ; T <sub>8</sub>	[40,44,49–51]
5	1120	$\nu_{\text{ring-s}}$ (Si-O-Si), LO mode	(SiO) <sub>4</sub> ; T <sub>7</sub> , Sld	[49]
6	1085	$\nu_{\text{as}}$ (C=C)	Si-Ph-Cl	[48]
7	1050	$\nu_{\text{as}}$ (Si-O-Si), TO mode	(SiO) <sub>4</sub> , Sld	[40,44,49,51]
8	1030	$\nu_{\text{as}}$ (Si-O-Si), TO mode	(SiO) <sub>6</sub>	[40,44]
9	1015	$\nu_{\text{s}}$ (C=C)	Si-Ph-Cl	[48]
10	1005	$\nu_{\text{as}}$ (Si-O-Si)	Lineal siloxane	[50]
11	950	$\nu$ (Si-O <sup>-</sup> /Si-OH)	Si-OH	[40,44,46]
12	815	T <sub><math>\delta,y</math></sub> C-H	Si-Ph-Cl	[36,48]
13	760	$\Phi$ C-H	Si-Ph-Cl	[36]
14	710	C-Cl	Si-Ph-Cl	[36,47]

$\nu$ , Stretching vibration;  $\nu_{\text{s}}$ , Symmetric stretching vibration,  $\nu_{\text{as}}$ , Asymmetric stretching vibration;  $\nu_{\text{ring-s}}$ , Antiparallel displacements of O atoms on opposite sides of a (SiO)<sub>x</sub> ring;  $\nu_{\text{ring-as}}$ , Parallel displacements of O atoms on opposite sides of a (SiO)<sub>x</sub> ring; T <sub>$\delta,y$</sub>  C-H, Wagging out and inside the plane;  $\Phi$ , Deformation out and inside the plane; LO, Longitudinal optical vibration mode; TO, Transversal optical vibration mode; (SiO)<sub>4</sub>, 4-fold ring; (SiO)<sub>6</sub>, 6-fold ring; T<sub>7</sub>, Open cage-like silsesquioxane; T<sub>8</sub>, Cage-like silsesquioxane; Sld, Ladder-like silsesquioxane.

The bands due to the vibrations of  $\nu_{\text{as}}$  (Si-O-Si) in the spectral range of 1400–1000  $\text{cm}^{-1}$  (Table 1) correspond to simple structures (linear siloxane chains and (SiO)<sub>4</sub> or (SiO)<sub>6</sub> rings) and more compact and complex structures (i.e., polyhedral oligomers of silsesquioxanes, POSS). Oligomers known as open or closed cages (T<sub>7</sub> and T<sub>8</sub>, respectively) and short ladders (SLd) are among the best known POSS, which are formed by the fusion of two or more four-membered rings ((SiO)<sub>4</sub>) (Figure 4) [52–56].

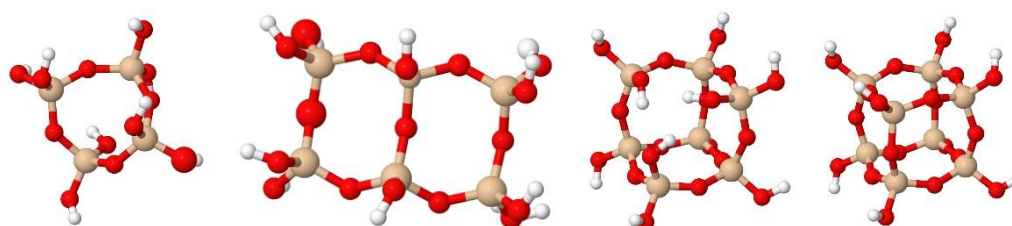


**Figure 4.** From left to right: 4-fold ring, short ladder (SLd), open-cage (T<sub>7</sub>), and close-cage (T<sub>8</sub>).

The formation of the rings that constitute these structures ((SiO)<sub>4</sub>) is thermodynamically favored in the oligomerization of siloxanes in acidic media [45,57], in contrast to the six-membered rings ((SiO)<sub>6</sub>), kinetically favored and typical of amorphous materials [39,58]. To study how the precursor affects the formation of ordered structures, it is necessary to know the proportion of (SiO)<sub>4</sub> in the silica matrix. For this purpose, the deconvolution of the FT-IR spectra in the range of 1300–980 cm<sup>-1</sup> was performed using the non-linear least-squares method, obtaining the Gaussian–Lorentzian components. The different distances and degrees of torsion of Si–O–Si bonds in (SiO)<sub>4</sub> and (SiO)<sub>6</sub> rings allow us to distinguish bands belonging to the optical modes of vibration; two in transverse mode between 1100 and 1000 cm<sup>-1</sup> (TO<sub>4</sub> and TO<sub>6</sub>) and two in longitudinal mode between 1250 and 1100 cm<sup>-1</sup> (LO<sub>4</sub> and LO<sub>6</sub>) [40,44,59,60]. In this work, a modification of this method has been carried out, consisting of the adjustment of additional bands (Table 1) corresponding to (i) C=C and C-H vibrations of the chlorophenyl (1450–700 cm<sup>-1</sup>); (ii) vibrations of the siloxane groups and Si-O bonds, characteristic of amorphous silica (950 and 800 cm<sup>-1</sup>, respectively); (iii) vibrations of the (SiO)<sub>4</sub> rings that make up the POSS:  $\nu_{\text{ring-s}}$  and  $\nu_{\text{ring-as}}$  for the “open” species (T<sub>7</sub> and short ladders), and only  $\nu_{\text{ring-as}}$  for the “closed” species (T<sub>8</sub>), due to the  $\nu_{\text{ring-s}}$  vibration mode being forbidden [49]; and (iv)  $\nu_{\text{as}}$  (Si–O–Si) vibration of linear siloxanes. As an example, the calculated spectra and the bands generated for the reference xerogel and 100CIPh are displayed in Figure 5. The calculated bands and the fit of 5CIPh, 10CIPh, 15CIPh, and the two phases of 20CIPh are depicted in Figure S3 of the Supplementary Material.

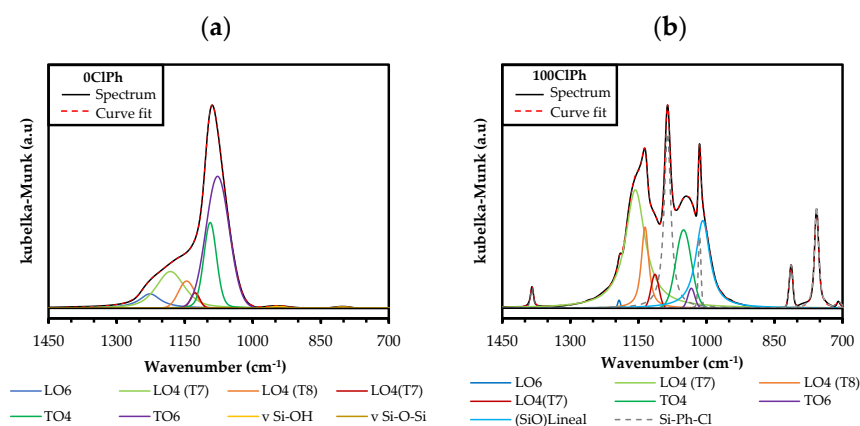


**Figure 5.** Experimental and calculated spectra of (a) reference and (b) 100CIPh.

The percentage area of each component and the residual value (difference between the real spectrum and the fit) are exhibited in Table S1 of the Supplementary Material. The percentage of four-membered and six-membered rings was determined by applying the following equations to the Gaussian–Lorentzian bell areas of the TO and LO components:

$$(\text{SiO})_6, \% = \frac{A(\text{LO}_6) + A(\text{TO}_6)}{A(\text{LO}_4) + A(\text{TO}_4) + A(\text{LO}_6) + A(\text{TO}_6)} \times 100 \quad (1)$$

$$(\text{SiO})_4, \% = \frac{A(\text{LO}_4) + A(\text{TO}_4)}{A(\text{LO}_4) + A(\text{TO}_4) + A(\text{LO}_6) + A(\text{TO}_6)} \times 100 \quad (2)$$

where  $A(\text{LO})_6$  is the area of the band at 1190 cm<sup>-1</sup>,  $(\text{TO})_6$  is the area of the band at 1030 cm<sup>-1</sup>,  $A(\text{LO})_4$  is the sum of the areas of the three LO<sub>4</sub> bands, 1160, 1135, and 1120 cm<sup>-1</sup>, and  $A(\text{TO})_4$  is the area of the band at 1050 cm<sup>-1</sup>. Table 2 displays the proportion of rings calculated by applying Equations (1) and (2). It can be observed that increasing the molar percentage of CIPhTEOS in the xerogels favors the formation of (SiO)<sub>4</sub> rings (from 46.54% in the reference to 97.35% in 100CIPh).

**Table 2.** Proportion of (SiO)<sub>4</sub> and (SiO)<sub>6</sub> rings in the hybrid materials.

Hybrid Material	LO <sub>6</sub>	LO <sub>4</sub>	TO <sub>4</sub>	TO <sub>6</sub>	(SiO) <sub>4</sub>	(SiO) <sub>6</sub>
	(%)				(%)	
0CIPh	7.0	28.5	18.1	46.5	46.5	53.5
5CIPh	26.7	31.8	38.6	3.0	70.4	29.6
10CIPh	12.8	43.9	29.8	13.6	73.7	26.3
15CIPh	12.3	43.1	33.9	10.7	77.0	23.0
20CIPh (Monolith)	3.3	13.4	30.9	52.4	44.3	55.7
20CIPh (Precipitate)	2.6	21.0	68.3	8.1	89.6	10.8
100CIPh	0.4	77.2	20.2	2.3	97.4	2.7

Another noteworthy observation is the great difference in the percentage of these rings between both phases of 20CIPh: The monolithic phase has a percentage of rings similar to that of the reference 0CIPh, and the phase that precipitates is similar to 100CIPh. This might be explained by taking into account that an increase in CIPhTEOS favors the formation of POSS, which are mainly formed by four-membered rings, and, as their abundance increases, there is a critical point at which these species exceed the molar solubility in the reaction media and segregate as a precipitate [61].

## 2.2. <sup>29</sup>Si Nuclear Magnetic Resonance (NMR)

<sup>29</sup>Si NMR spectra of the hybrid materials were obtained to determine the relationship between the molar percentage of the precursor and the relative abundance of silicon species in the xerogels. Figure 6a depicts the spectra of the hybrid materials normalized with respect to the signal of the dominant species, Q<sup>3</sup>, the most intense in all cases.

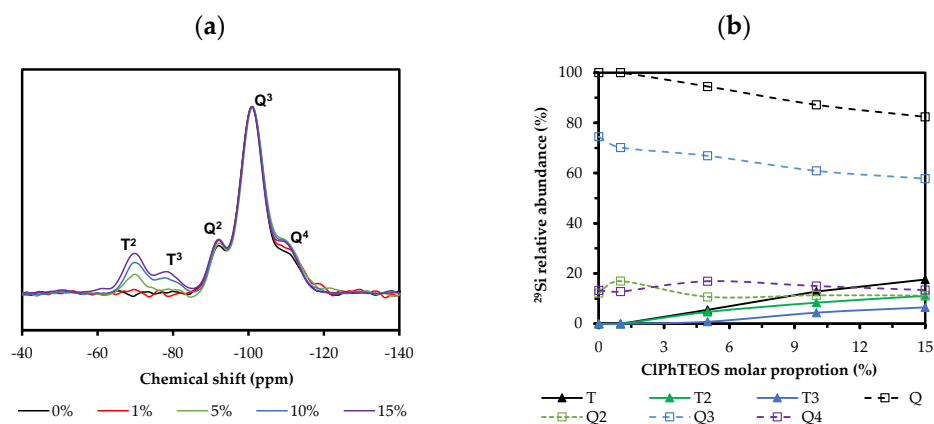


**Figure 6.** (a) Normalized <sup>29</sup>Si NMR spectra of the hybrid xerogels. (b) Variation of the relative abundance of the condensed species with respect to the percentage of CIPhTEOS.

The signals associated with the less condensed species (Q<sup>1</sup> and T<sup>1</sup>) in Figure 6a are not observed. The dominant species corresponding to the hybrid precursor is the semi-condensed T<sup>2</sup>, whose intensity is greater than that of the more condensed T<sup>3</sup> in all the materials. In addition, Figure 6b displays both the evolution of the relative abundance of Q (Q<sup>2</sup> + Q<sup>3</sup> + Q<sup>4</sup>) and T (T<sup>2</sup> + T<sup>3</sup>) species with respect to the molar percentage of CIPhTEOS, as well as that of each species. For example, the Q<sup>2</sup> relative abundance increases slightly to stabilize at 11% and Q<sup>4</sup> increases up to 5% CIPhTEOS and then decreases at higher molar percentages of organic precursor. Table 3 exhibits the chemical shifts of each <sup>29</sup>Si species in the spectra and the integrals of the T species.

**Table 3.** Chemical shifts and integral areas of the  $^{29}\text{Si}$  NMR spectra of the hybrid materials.

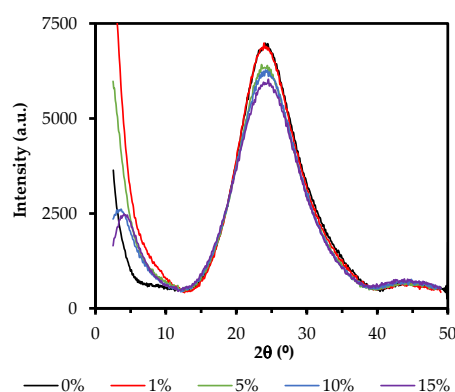
Xerogel	$^{29}\text{Si}$ NMR (ppm)					Band Areas			
	T <sup>2</sup>	T <sup>3</sup>	Q <sup>2</sup>	Q <sup>3</sup>	Q <sup>4</sup>	T	T <sup>2</sup>	T <sup>3</sup>	T <sup>3</sup> /T <sup>2</sup>
0CIPh	a	a	−92.1	−100.9	−109.0	a	a	a	-
1CIPh	a	a	−92.3	−101.0	−109.3	a	a	a	-
5CIPh	−69.8	−78.7	−92.3	−101.1	−109.4	5.5	4.7	0.8	0.2
10CIPh	−69.8	−79.1	−92.2	−101.0	−108.5	12.8	8.4	4.4	0.5
15CIPh	−69.8	−78.2	−92.1	−100.9	−108.6	17.6	11.1	6.5	0.6

<sup>a</sup> Non detected.

There is no significant displacement of the chemical shifts with the increase in CIPh-TEOS, indicating that the environment of the silicon atoms does not change substantially. The chemical shifts of the T signals (organic precursor) are less negative than those of the Q signals (TEOS) because the chlorophenyl moiety removes less electronic charge from the silicon atom than oxygen, favoring the Shielding Effect [62,63]. Additionally, a higher positive charge density in the silicon atom favors nucleophilic attacks and therefore condensation [64,65]; however, the more abundant species is the least condensed and not T<sup>3</sup>, indicating that the inductive effect exerted by the chlorine atom of the chlorophenyl moiety is weaker than its steric effect, preventing total condensation in the materials. The increase in T<sup>3</sup> species is related to the presence of POSS in the material, since the silicon atoms that form (SiO)<sub>4</sub> rings are mainly condensed species T<sup>3</sup>, Q<sup>3</sup>, or Q<sup>4</sup> (less condensed structures T<sub>7</sub> and SLd also contain T<sub>2</sub> and Q<sub>2</sub>) [49]. In fact, the shifts of T<sup>3</sup> species (Table 3) are closer to those observed in T<sup>8</sup> structures (−77 ppm) than to those of the aliphatic R-Si-O<sub>1.5</sub> species (−66 to −67 ppm) [66,67]. Finally, it is worth mentioning that 100CIPh material only contains T units and, as has been verified in the analysis of its FT-IR spectra, it is composed almost exclusively of (SiO)<sub>4</sub> rings.

### 2.3. X-ray Diffraction (XRD)

Figure 7 depicts the X-ray diffraction patterns of the hybrid materials synthesized at different molar percentages of organic precursor.

**Figure 7.** XRD diffractograms of the hybrid xerogels (reference, 1CIPh, 5CIPh, 10CIPh, and 15CIPh).

All the diffractograms showed a broad diffraction maximum at  $2\theta \sim 24^\circ$ , characteristic of the amorphous silica and associated with the distance between the silicon atoms linked by siloxane bridges [68]. This maximum slightly decreases with the increase in the molar percentage of the organic precursor. Interestingly, another maximum can be observed at  $2\theta < 10^\circ$  when the molar percentage of the precursor is increased (10CIPh and 15CIPh). This new diffraction maximum is associated, in the literature, with the presence of ordered domains composed of POSS in the form of cages (T<sub>7</sub> or T<sub>8</sub>) or short ladders within the amorphous matrix of the material [60]. The emergence of this maximum as the one at  $24^\circ$  decreases is consistent with the greater local structuration of the materials as we increase the

molar percentage of the organic precursor. This behavior was already seen in previously studied CIRTEOS xerogels (R = M, methyl; E, ethyl, or P, propyl), where it was found that the maximum at  $2\theta < 10^\circ$  appeared at lower molar percentages than their analogous RTEOS. In these chlorinated series, the minimum molar percentages containing the new maximum were 30, 1, and 10% for CIMTEOS, CIETEOS, and CIPTEOS, respectively [37]. The CIPhTEOS series not only share this minimum percentage with the CIPTEOS but also have more  $T^2$  than  $T^3$  species, which could indicate that, although the chlorine atom in the precursors favors the condensation and the subsequent formation of POSS, the steric effect of the bulkier organic moieties (both propyl and phenyl) could generate less condensed POSS, such as  $T_7$  or SLd. In all the patterns, another low-intensity maximum is observed around  $45^\circ$ , which is associated, according to Bragg's law ( $n = 2$  in  $n\lambda = 2d \sin \theta$ ), with a replica of the maximum at  $2\theta \sim 24^\circ$ , indicating long-range order in the materials. Table 4 displays the angles, intensities, and distances calculated from Bragg's law for each maximum in the diffractograms of Figure 5.

**Table 4.** Bragg angles ( $2\theta$ ), band area (A), and bond distance ( $d_1$  and  $d_2$  (nm)) calculated from XRD maxima of hybrid xerogels at different molar percentages of organic precursor (CIPhTEOS).

Xerogel	Peak $2\theta < 10^\circ$			Peak $10^\circ > 2\theta < 30^\circ$		
	$2\theta_1$ ( $^\circ$ )	$A_1$	$d_1$ (nm)	$2\theta_2$ ( $^\circ$ )	$A_2$	$d_2$ (nm)
0CIPh	a	a	a	24.11	6481	0.369
1CIPh	a	a	a	23.93	6845	0.372
5CIPh	a	a	a	23.58	5921	0.377
10CIPh	3.6	2112	2.43	24.14	5778	0.369
15CIPh	4.1	1985	2.17	24.53	5534	0.363

<sup>a</sup> Non detected.

In 1CIPh and 5CIPh materials, the Si–O–Si bond elongates proportionally to the molar percentage of the precursor (maximum shifts to smaller angles), consistent with what was observed in the  $^{29}\text{Si}$  NMR spectra, that is, the increase in T species (from the organic precursor) causes a decrease in the average positive charge density of the silicon atoms, and therefore, the siloxane bonds are less polarized. However, as the molar percentage of the organic precursor increases in 10CIPh and 15CIPh, the bond becomes shorter (the maximum shifts to higher angles). This effect, inverse to the one discussed above, is related to the appearance of a diffraction maximum at  $2\theta < 10^\circ$  in 10CIPh and 15CIPh, since this maximum is associated with ordered POSS-type structures, where the siloxane bridges (Si–O–Si) that make up the  $(\text{SiO})_4$  rings are more compact than those of the amorphous silica (formed mainly by  $(\text{SiO})_6$ ) [40], thus explaining the decrease in Si–O–Si distances associated with the maximum at  $2\theta \sim 24^\circ$ . The calculated distances for the additional maximum at  $2\theta < 10^\circ$  (displayed in Table 4) are similar to those associated with the organic moiety in the cage-like structures (1–3 nm) [39,54], and to that of the interplane between short ladders [56,69]. Additionally, the X-ray diffractogram of 100CIPh is depicted in Figure S4 (Supplementary Material). In the diffractogram, a sharp and intense diffraction maximum at  $2\theta = 6.84^\circ$  (1.3 nm) can be observed, which confirms that the 20CIPh precipitate contains a large amount of POSS. In a recent study, Nowacka et al. reported an interplane distance of 1.24 nm for ladder-like phenylsilsesquioxane oligomers, suggesting that these are the species formed in 100CIPh [60].

#### 2.4. Helium Pycnometry

Helium pycnometry reveals the skeletal density of the synthesized xerogels. Figure 8 depicts the variation in the skeletal density as a function of the molar percentage of CIPhTEOS.



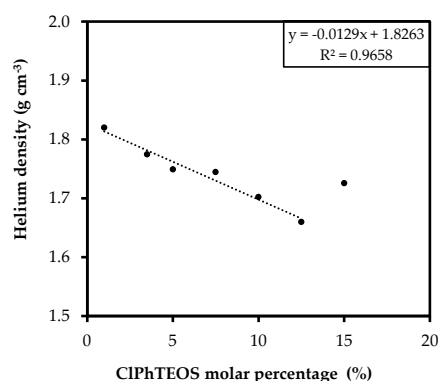


**Figure 8.** Skeletal density of the hybrid materials with respect to the percentage of CIPhTEOS.

A decrease in the skeletal density with respect to CIPhTEOS is observed, since the organic precursor blocks one of the hydrolysis and condensation positions, thus reducing the degree of cross-linking with respect to the reference material (100% tetraethoxysilane, TEOS). The skeletal density of 15CIPh is greater than expected, which indicates that the limit of precursor that the system can assimilate has been reached. This new series has lower values of skeletal density than the previously studied CIRTEOS series (R = methyl, M; ethyl, E; propyl, P). For example, for 10CIPh, the skeletal density is 1.68 in contrast to 1.91, 1.85, and 1.80 g cm<sup>-1</sup> for CIMTEOS, CIPTEOS, and CIETEOS, respectively [37]. This result is consistent with the information deduced from the <sup>29</sup>Si NMR spectra and the XRD diffractograms (CIPhTEOS favors the less condensed POSS, T<sub>7</sub> and SLd).

### 2.5. N<sub>2</sub> and CO<sub>2</sub> Adsorption Isotherms

N<sub>2</sub> and CO<sub>2</sub> molecules have a similar size; however, the temperature at which the adsorption takes place is very different, being −196 °C for N<sub>2</sub> isotherms and 0 °C for CO<sub>2</sub> isotherms. If the pores are very thin, N<sub>2</sub> molecules cannot access them due to kinetic restrictions; however, CO<sub>2</sub> molecules can. On the other hand, the high saturation pressure of CO<sub>2</sub> vapor (3.5 MPa) allows the finer microporosity to be explored in detail, which is covered at very low relative pressures. This fact makes the data provided by both isotherms complementary and makes it possible to differentiate the micropores of less than 0.7 nm and even the finest mesopores. If there are no kinetic constraints, N<sub>2</sub> adsorption provides the volume of pores of less than 50 nm, CO<sub>2</sub> adsorption of those sized less than 0.7 nm, and the difference of these values would provide the microporosity between 2 and 0.7 nm. This divergence can be explained by the different adsorption mechanisms taking place in both microporous intervals; in the so-called “primary micropore filling”, the ultramicropores are accessed at a very low relative pressure ( $p/p_0 = 0.03$ ) and the adsorbent–adsorbate interactions predominate over those of the adsorbate–adsorbate, whereas, in wider micropores, the adsorbate–adsorbate interactions predominate, favoring a cooperative process of adsorption [70,71].

The N<sub>2</sub> adsorption isotherms (at −196 °C) and the CO<sub>2</sub> isotherms (at 0 °C) of the hybrid xerogels are shown in Figure 9. The isotherm of the reference material has an open knee, a sign of a wide micropore size distribution, characteristic of type I(b) isotherms. Moreover, its slope is pronounced in the adsorption, and it presents a hysteresis loop in the desorption (H2(a)), which is characteristic of a type IV isotherm typical of mesoporous materials. Therefore, the reference material can be considered micro-mesoporous with a type I(b)-IV(a) mixed isotherm [71]. Except for 1CIPh and 15CIPh materials, the higher the percentage of an organic precursor the smaller the pore volume, obtaining a type I(a) isotherm in all cases, typical of microporous materials with a narrow pore distribution. The isotherm of 1CIPh is a type IV(a) with an H1 hysteresis loop, indicating that, in this case, the organic precursor increases the total volume of pores and mesopores with respect to the reference, an effect that was also observed in analogous hybrid materials previously reported, which is associated with a change in the morphology of the pores, from cone-

shaped to inkwell-shaped pores [27,37]. The 15CIPh isotherm is type I(a) but, surprisingly, it adsorbs more N<sub>2</sub> than 10CIPh, 7.5CIPh, and CIPh5. This fact is consistent with the value obtained for its skeletal density (Figure 8), which suggests that in this material, the limit of the organic precursor that the xerogel accepts is practically reached and is therefore heterogeneously distributed in the silicon matrix. Table 5 exhibits the textural parameters obtained from the adsorption isotherms.

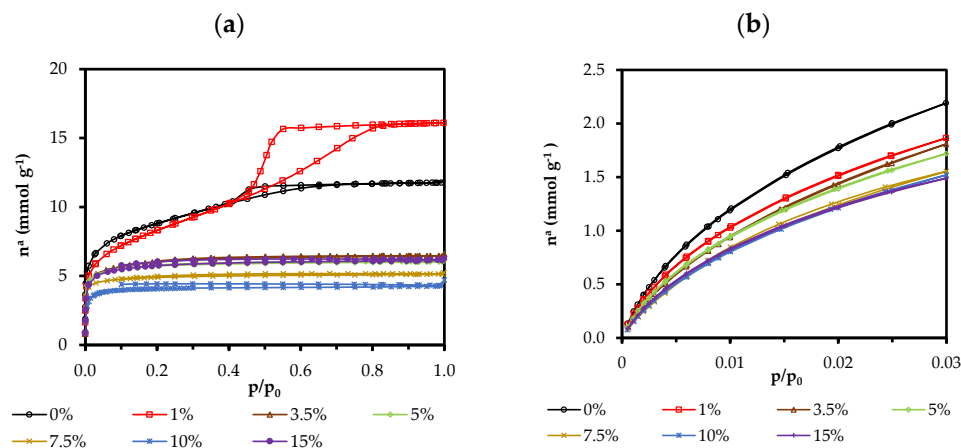


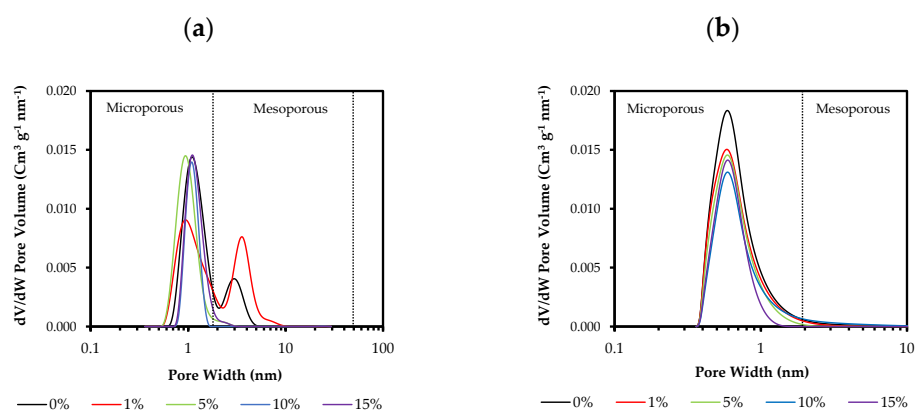
Figure 9. Isotherms of the hybrid xerogels: (a) N<sub>2</sub> (−196 °C), and (b) CO<sub>2</sub> (0 °C).

Table 5. Textural parameters of the hybrid xerogels.

Xerogel	a <sub>BET</sub>	a <sub>DR</sub>	V <sub>micro</sub>	V <sub>micro</sub>	V <sub>meso</sub>	V <sub>total</sub>	BJH APS <sup>a</sup>	E <sub>c</sub> <sup>b</sup>	E <sub>c</sub> <sup>b</sup>	
	(N <sub>2</sub> )	(CO <sub>2</sub> )	(N <sub>2</sub> )	(CO <sub>2</sub> )	(N <sub>2</sub> )	(N <sub>2</sub> )		(N <sub>2</sub> )	(N <sub>2</sub> )	(CO <sub>2</sub> )
	(m <sup>2</sup> g <sup>−1</sup> )	(m <sup>2</sup> g <sup>−1</sup> )	(cm <sup>3</sup> g <sup>−1</sup> )	(cm <sup>3</sup> g <sup>−1</sup> )	(cm <sup>3</sup> g <sup>−1</sup> )	(cm <sup>3</sup> g <sup>−1</sup> )		(nm)	(KJ mol <sup>−1</sup> )	(KJ mol <sup>−1</sup> )
0CIPh	697	510	0.283	0.195	0.074	0.407	3.61	15.27	19.71	
1CIPh	656	426	0.253	0.163	0.222	0.557	4.38	15.57	19.97	
3.5CIPh	504	429	0.205	0.164	0.007	0.223	3.33	18.73	19.28	
5CIPh	493	400	0.205	0.153	0.006	0.209	3.40	18.11	19.77	
7.5CIPh	431	388	0.176	0.148	0.004	0.177	3.29	19.49	18.92	
10CIPh	367	363	0.151	0.139	0.003	0.147	2.05	16.24	19.29	
15CIPh	497	358	0.208	0.137	0.007	0.212	3.11	15.61	19.55	

<sup>a</sup> Average Pore Size from desorption loop; <sup>b</sup> Characteristic energy from Dubinin–Raduskevich.

A decrease in the specific surface area (a<sub>BET</sub>) with the increase in the molar percentage of CIPhTEOS is observed, except for 15CIPh, which has a larger area than expected. Additionally, the table displays the volume of micropores obtained from the N<sub>2</sub> adsorption data (V<sub>micro</sub>(N<sub>2</sub>)), and of the narrowest micropores (V<sub>micro</sub>(CO<sub>2</sub>), where φ < 0.7 nm), determined by applying the Dubinin–Raduskevich equation to the CO<sub>2</sub> adsorption data. Both volumes decrease with an increase in the molar percentage of CIPhTEOS. The average pore size determined by the Barrett–Joyner–Halenda method (BJH APS) indicates that their mesoporosity narrows with the molar percentage of CIPhTEOS until microporous materials are obtained. In comparison with the CIRTEOS materials with the same percentage of the organic precursor, 10CIPh has a higher surface area and V<sub>micro</sub>(N<sub>2</sub>) than those of CIPhTEOS and ClhTEOS, but lower than that of CIMTEOS [37]. This implies, once again, that these materials are less condensed due to the predominance of T<sup>2</sup> over T<sup>3</sup> species and the bulky nature of the chlorophenyl group. Figure 10 depicts the pore size distribution by applying DFT calculations to the N<sub>2</sub> and CO<sub>2</sub> isotherm data.



**Figure 10.** Pore size distribution of the materials calculated from (a)  $N_2$  isotherms and (b)  $CO_2$  isotherms.

All the materials are microporous, with an internal width close to 1 nm (Figure 10). The distribution shows that the materials do not present a significant volume of mesopores, except for the reference and 1ClPh.

## 2.6. Microscopy

### 2.6.1. Field-Emission Scanning Electron Microscopy (FE-SEM)

To determine the influence of the precursor on the texture, micrographs of the materials were acquired using scanning electron spectroscopy (SEM). The micrographs of the whole series are displayed in Figure 11.

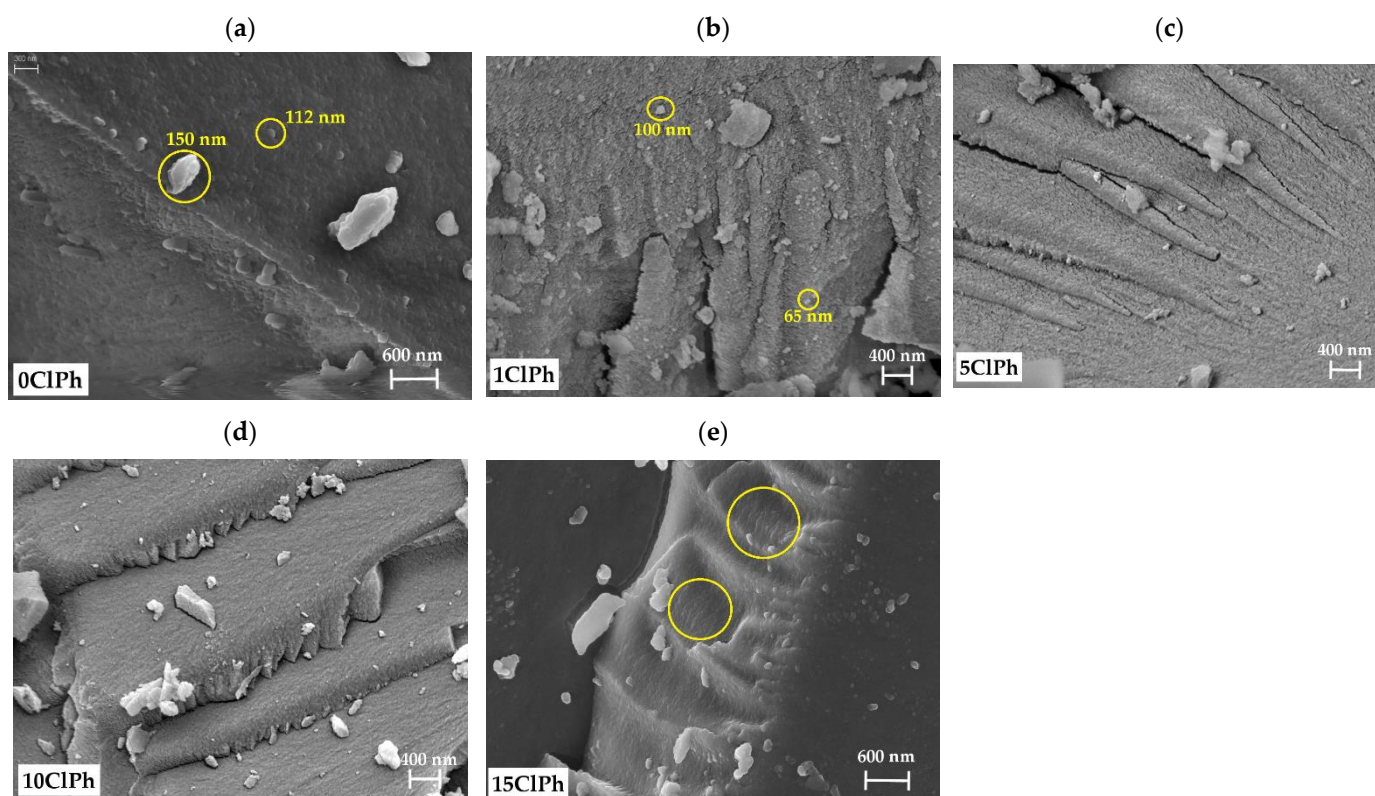


**Figure 11.** FE-SEM micrographs of: (a) 0ClPh, (b) 1ClPh, (c) 5ClPh, (d) 10ClPh, and (e) 15ClPh.

The micrograph of the reference material (Figure 11a) exhibits a rough morphology composed of small intersecting globular particles in a chainmail-like surface (110–150 nm). The space between the particles corresponds to the narrow mesoporosity of this material, consistent with the  $N_2$  adsorption isotherm. Figure 11b shows how the use of only 1% of the

organic precursor in the synthesis of 1CIPh results in a remarkable change: The surface is rougher, and the constituent particles are smaller (30–100 nm), justifying why the isotherm of this material reflects a greater specific surface area and mesoporosity than the reference material (0CIPh). In Figure 11c,d, respectively, CIPh5 and CIPh10 display a progressive smoothing of the surface with the increase in the organic precursor, which is consistent with the loss of mesoporosity and pore volume reduction deduced from their isotherms. A stratification of the surface can also be observed in overlapped compacted sheets to give mainly microporous materials. In CIPh15 (Figure 11e), the layers of compacted sheets, which are related to the stacking of the ladder POSS [56], can be better appreciated.

### 2.6.2. High Resolution-Transmission Electron Microscopy (HR-TEM)

Figure 12 displays TEM micrographs of the hybrid materials.

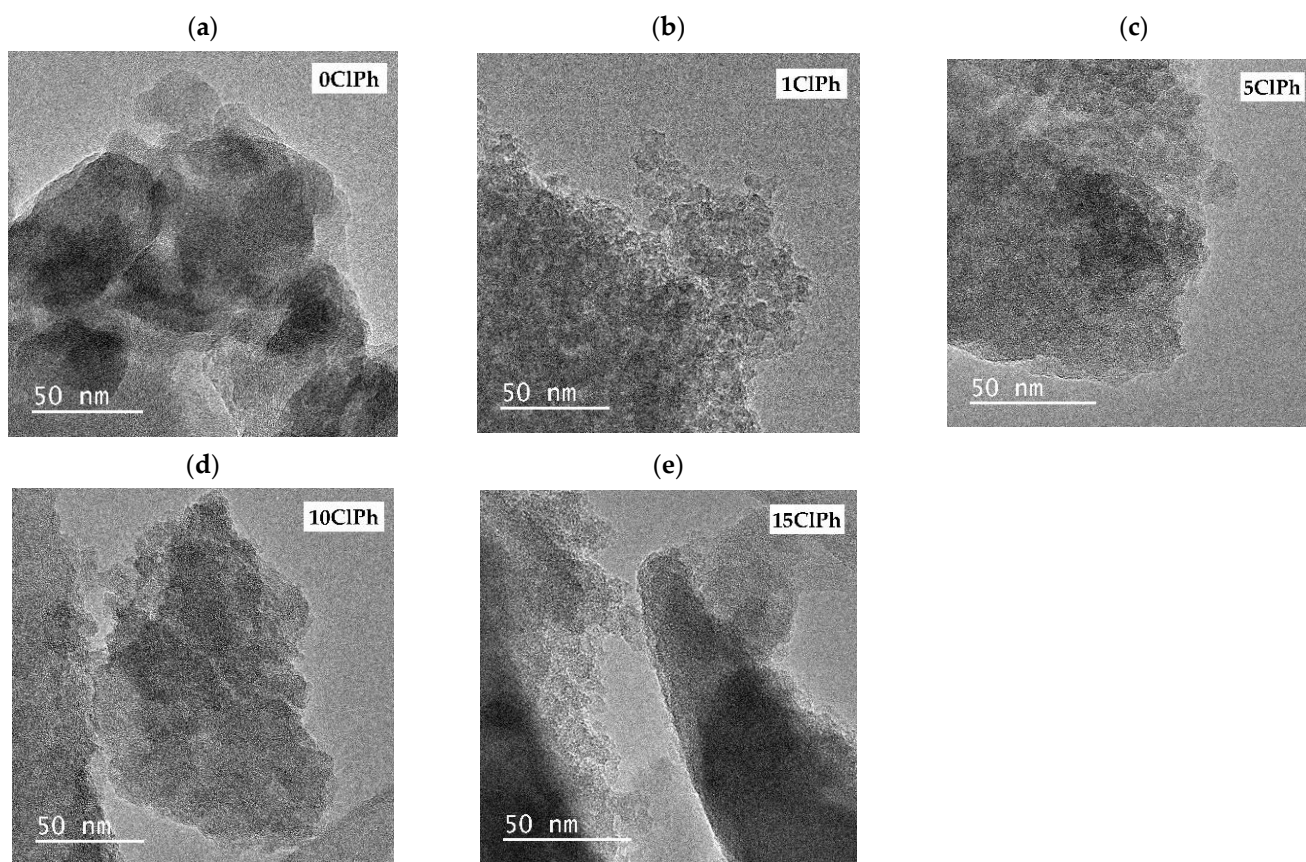


**Figure 12.** HR-TEM micrographs of (a) 0CIPh, (b) 1CIPh, (c) 5CIPh, (d) 10CIPh, and (e) 15CIPh.

The micrograph of the reference material (Figure 12a) exhibits a morphology formed by an agglomerate of large particles of several tens of nm, which leave holes that are related to the mesoporosity of the material. In the following micrograph (Figure 12b, 1CIPh), particles of smaller size are interconnected, but they are still identifiable, unlike in the micrographs of the materials with a higher percentage of CIPhTEOS. To determine the degree of precursor distribution in the material, a mapping of the weight percentage of chlorine in the materials was carried out by X-ray energy dispersion. Table 6 displays the experimental and theoretical weight percentage of chlorine obtained for each material.

**Table 6.** Average weight percentage of chlorine determined theoretically and by EDX of the hybrid materials.

Xerogels	Weight Percentage of Chlorine		E/T
	(wt%)		
	Theoretical (T)	Experimental (E)	
1CIPh	0.37	0.29	0.77
5CIPh	1.68	1.20	0.72
10CIPh	2.97	2.80	0.94
15CIPh	3.99	2.28	0.57

The weight percentages of chlorine in Table 6 are the average of the values recorded in different particles of the sample and reflect that the actual content of chlorine in the materials is lower than the theoretical. However, most of the chlorophenyl precursor is found as part of 1CIPh, 5CIPh, and 10CIPh materials, in contrast to 15CIPh, where approximately half of the amount of precursor used for the synthesis is present in the material. This is consistent with what was observed in the rest of the characterization techniques, since the results obtained are characteristic of a material with a lower molar percentage of the organic precursor than the actual amount used for its preparation.

### 3. Conclusions

A new series of hybrid xerogels have been prepared via the co-condensation of TEOS and CIPhTEOS as the organic precursor at different molar percentages. From the FT-IR spectra of the materials and by applying a deconvolution method, the percentages of  $(\text{SiO})_6$  and  $(\text{SiO})_4$  rings in the silica matrix of the materials were determined, the former associated with amorphous silica and the latter with ordered structures such as polysilsesquioxanes (POSS). The study determined that increasing the molar percentage of the organic precursor leads to an increase in the proportion of four-membered rings,  $(\text{SiO})_4$ . The presence of POSS is consistent with the XRD diffractograms, where an additional maximum at  $2\theta < 10^\circ$  associated with ordered domains is observed for the materials with the highest CIPhTEOS content. The  $^{29}\text{Si}$  NMR spectra indicate that the most abundant silicon species from the organic precursor (T) are the semi-condensed ( $\text{T}^2$ ), likely due to the steric and electronic effect exerted by the chlorophenyl groups during the crosslinking of the colloids. Regarding the textural properties, it has been determined that an increase in the organic precursor in the materials results in a loss of mesoporosity and specific surface area, and a narrower pore size distribution. This is closely related to the smoothing of the material's surface and the decrease in particle size observed in the FE-SEM and HR-TEM when increasing the molar percentage of CIPhTEOS. It is suggested that the layers that the micrographs exhibit are due to the stacking of the less condensed POSS ( $\text{T}_7$  open cages and short ladders), whereas condensed ones ( $\text{T}_8$  close cages) containing only hydrophobic chlorophenyl groups in their  $\text{T}^3$  silicon atoms precipitate and cause the heterogeneity observed in the 20CIPh material. In fact, the aromatic moiety together with the electronic properties of the chlorine atom opens the door to a more specific interaction with volatile aromatic compounds, and thus, for the application of these materials in sensorics for the detection of pollutants in the atmosphere. The study of the chemical and textural properties of these novel hybrid materials is the prelude to their use in different relevant fields. In fact, the aromatic moiety together with the electronic properties of the chlorine atom opens the door to a more specific interaction with volatile aromatic compounds, and thus, to the application of these materials in sensorics for the detection of pollutants in the atmosphere.

### 4. Materials and Methods

#### 4.1. Materials

The siliceous precursors TEOS (tetraethoxysilane, purity > 99%) and CIPhTEOS ((4-chlorophenyl) triethoxysilane, purity > 97%) were supplied by Sigma-Aldrich (San Luis,

MO, USA). Absolute ethanol (Emsure<sup>®</sup>) and hydrochloric acid (HCl, 37% *w/w*) were purchased from Merck (Darmstadt, Germany) and potassium bromide (FT-IR grade) from Sigma-Aldrich (San Luis, MO, USA). All chemicals were used as received without further purification.

#### 4.2. Synthesis of Silicon Hybrid Xerogels

Hybrid xerogels were prepared following the procedure described in previous works [37,72,73], where the molar ratio of (TEOS + CIPhTEOS): ethanol: water was fixed to 1:4.75:5.5 throughout the whole series, and the amounts of reagent and solvent were adjusted to obtain 20 mL of alcogels. The xerogels were named after the molar percentage used (i.e., 15CIPh for the xerogel with a molar percentage of 15%).

Briefly, TEOS and CIPhTEOS were mixed in a 30 mL vessel ( $\varphi$  3.5 cm, threaded plastic lid, Schrarlab, Barcelona, Spain). Then, absolute ethanol was added, followed by the dropwise addition of Milli-Q grade water under magnetic stirring to facilitate miscibility. Once the pH of the mixtures remained unchanged (after approximately 10 min), an automatic burette (Tritino mod. 702 SM, Metrohm, Herisau, Switzerland) was used to set the pH at 4.5 (0.05 M HCl), and the mixture was stirred for 10 min to ensure homogenization. The closed vessels were placed in a thermostated oven at 60 °C (J.P. Selecta S.A, Barcelona, Spain) until gelation (considered the time when the shape of the materials did not change when the vessel was tilted). Subsequently, 5 mL of ethanol was added to cure the alcogel at room temperature for one week. Next, the vessels were opened and covered with parafilm<sup>TM</sup>, perforated with holes to facilitate solvent evaporation, and dried at room temperature under atmospheric pressure. The monolith was considered dried when no significant variation in its mass was observed. Finally, the xerogels were further dried (90 °C under vacuum) and then ground in an agate mortar.

#### 4.3. Characterization of Silicon Hybrid Xerogels

Various techniques have been applied to characterize the structure of the hybrid materials due to their amorphous nature [74]. FT-IR spectra were acquired using a Jasco spectrometer (mod. 4700, Japan). Two spectra were obtained for each sample: (i) In the range of 4000–2200  $\text{cm}^{-1}$ , using 2 mg of the sample to obtain information on the –OH groups and aromatic C–H bonds, and (ii) in the range of 2200–400  $\text{cm}^{-1}$  using 0.6 mg of the sample to avoid saturation of the Si–O–Si asymmetric stretching signal [75]. Tablets were dispersed in KBr and dried overnight. Spectra were recorded using 25 scans and a resolution of 4  $\text{cm}^{-1}$ . The absorbance was transformed into Kubelka–Munk units with the internal software of the spectrometer (Spectramanager, SMII FTIR Rev 216A ver2.15A) for the deconvolution of the spectra [44]. The method was modified to generate a maximum of fourteen Gaussian–Lorentzian bands in the 1450–700  $\text{cm}^{-1}$  spectral range, with a maximum of 200 interactions and a fixed baseline.

<sup>29</sup>Si Cross Polarization Magic-Angle Spinning (CP MAS) solid-state NMR was recorded on a Bruker AV-400 MHz spectrometer (Billerica, MA, USA) operating at 79.5 MHz. Chemical shifts were given in parts per million using TMS as the reference. The spectra were obtained <sup>1</sup>H decoupled, with a frequency of rotation of 5 kHz and 800 scans per spectrum. For the <sup>29</sup>Si NMR studies, classical notation was employed: T notation for silicon atoms from the organic precursor (bonded to three oxygens capable of forming siloxane bridges), and Q notation for silicon atoms from TEOS (bonded to four oxygens that can yield siloxane bridges). To describe the number of Si–O–Si bridges in each silicon atom, T and Q notations were completed with a superscript *i* (T<sup>*i*</sup>, *i* = 0, 1, 2 or 3; Q<sup>*i*</sup>, *i* = 0, 1, 2, 3 or 4) [62].

X-ray diffractograms were obtained using a PANalytical Empyrean XRD instrument (Empyrean, Almelo, The Netherlands) with a copper rotating anode and a graphite monochromator (at 45 kV and 40 mA) to select the CuK <sub>$\alpha$ 1/2</sub> wavelength at 1.54 nm. Measurements were performed in a stepped scan mode (steps of 0.013°), in the range of  $2 \leq 2\theta \leq 50^\circ$  at a rate of 0.5 steps  $\text{s}^{-1}$  [76].

A helium pycnometer was used to measure the skeletal density (AccuPyc 1330, Micromeritics, Norcross, GA, USA), performing 20 purges and 10 measurements for the initial calibration. The sample was weighed into a 1 cm<sup>3</sup> cell and analyzed using 10 purges and 5 measurements.

N<sub>2</sub> adsorption isotherms (at −196 °C with an isothermal jacket and immersed in a Dewar with liquid nitrogen) and CO<sub>2</sub> adsorption isotherms (at 0 °C in a thermostated recirculation bath using ethylene glycol as a refrigerant) were determined with a volumetric adsorption system (ASAP2020, Micromeritics, Norcross, GA, USA). First, 150 mg of sample was used for each isotherm, placed into a Pyrex glass tube, and degassed at 150 °C up to a residual vacuum of less than 0.66 Pa. The time needed for the analysis ranged from 14 to 55 h for N<sub>2</sub> adsorption and from 2.5 to 9 h for CO<sub>2</sub> adsorption. The recorded adsorption data were analyzed with the Microactive software (version 4.06), adjusting the parameters as appropriate for each model. Specific surface areas were calculated using two techniques: (i) The Brunauer–Emmett–Teller (BET) model ( $a_{\text{BET}}$ ), applying the Rouquerol criteria [77] and (ii) the Dubinin–Radushkevich (DR) method, applying a molecular section of 0.17 nm<sup>2</sup> to CO<sub>2</sub> ( $a_{\text{DR}}$ ) [78]. Pore volumes were defined by their diameter ( $\varphi$ ): (i) The volume of micropores ( $\varphi \leq 2$  nm) was obtained from the DR method ( $V_{\text{micro(N}_2)}$  and  $V_{\text{micro(CO}_2)}$ ), (ii) the volume of mesopores ( $2 < \varphi \leq 50$  nm) was calculated by abstracting the amount of N<sub>2</sub> adsorbed at  $p/p^\circ = 0.3$  from that adsorbed at  $p/p^\circ = 0.8$  ( $V_{\text{meso(N}_2)}$ ), and (iii) the total volume ( $V_{\text{Total(N}_2)}$ ) was considered the amount of N<sub>2</sub> adsorbed at  $p/p^\circ = 0.95$ . Liquid densities of the adsorbates were obtained from the literature (0.808 g cm<sup>−3</sup> for N<sub>2</sub> and 1.023 g cm<sup>−3</sup> for CO<sub>2</sub>) [70,79]. Porosity distributions were determined according to density-functional theory (DFT) using SAIEUS software and applying the “carbon-N2-77, 2D-NLDFT heterogeneous Surface” model for N<sub>2</sub> adsorption and the “carbon-CO2-273, 2D-NLDFT Het Surface, pp max = 10 atm” model for CO<sub>2</sub> adsorption. Mean pore sizes were further determined by applying the Barrett–Joyner–Halenda (BJH) method to the desorption curves, using a Kruk–Jaroniec–Sayari correction and thickness curve.

Field-emission scanning electron microscopy (FE-SEM) provides high-resolution images of sample surfaces. Micrographs were obtained with a Carl Zeiss SMT field emission scanning electron microscope (Carl Zeiss SMT, Oberkochen, Germany) at 200 kV.

High-resolution transmittance electron microscopy (HR-TEM) images were obtained at 200 kV with a JEOL 2000FXII microscope (Jeol Ltd., Tokyo, Japan) with a 0.28 nm point-to-point spatial resolution. The instrument was equipped with an Energy Dispersive X-Ray (EDX) INCA 200 spectrometer (Oxford Instruments, Abingdon, UK), which allowed the observation of the atomic distribution of carbon, silicon, and chlorine on the material.

**Supplementary Materials:** The following supporting information can be downloaded at: <https://www.mdpi.com/article/10.3390/gels8100677/s1>, Figure S1. FTIR spectra (range 4000–2750 cm<sup>−1</sup>) of the hybrid materials at different molar percentages and the reference (0CIPh); Figure S2. Photographs of the CIPhTEOS materials: (a) 0CIPh, (b) 15CIPh, (c) 20CIPh, and (d) 100CIPh; Figure S3. Calculated spectra and Gaussian–Laurentzian bands generated in the curve fitting for: (a) 5CIPh, (b) 10CIPh, (c) 15CIPh, (d) 20CIPh (monolith), and (e) 20CIPh (precipitate); Table S1. Wavelength and percentual area of the generated bands in the curve fitting for each CIPhTEOS material, and the curve fitting parameters; Figure S4. XRD pattern of 100CIPh.

**Author Contributions:** G.C.-Q.: investigation, writing—original draft. M.E.-V.: methodology, resources, writing—review and editing. M.V.L.-R.: Writing—review and editing. J.J.G.: Conceptualization, supervision, project administration, funding acquisition, writing—review and editing. All authors have read and agreed to the published version of the manuscript.

**Funding:** This research was funded by “Ministerio de Ciencia e Innovación” (Project ref. PID2020-113558RB-C42).

**Institutional Review Board Statement:** Not applicable.

**Informed Consent Statement:** Not applicable.

**Data Availability Statement:** The data presented in this study are available on request from the corresponding author.

**Acknowledgments:** The authors gratefully acknowledge the financial support received from “Ministerio de Ciencia e Innovación” from Spain (PID2020-113558RB-C42). G.C.-Q is thankful to “Ministerio de Universidades” of the Spanish government for the “Formación de Profesorado Universitario (FPU)” grant (FPU18/03467). The authors would also like to acknowledge the use of the “Centro de Instrumentación Científico-Técnica” at the University of Jaén, UCTAI at the Public University of Navarre and “Servicios Científico-Técnicos” at the University of Oviedo.

**Conflicts of Interest:** The authors declare no conflict of interest.

## References

1. Hannachi, Y.; Hafidh, A.; Ayed, S. Effectiveness of novel xerogels adsorbents for cadmium uptake from aqueous solution in batch and column modes: Synthesis, characterization, equilibrium, and mechanism analysis. *Chem. Eng. Res. Des.* **2019**, *143*, 11–23. [[CrossRef](#)]
2. Kobylinska, N.G.; Kessler, V.G.; Seisenbaeva, G.A.; Dudarko, O.A. In Situ Functionalized Mesoporous Silicas for Sustainable Remediation Strategies in Removal of Inorganic Pollutants from Contaminated Environmental Water. *ACS Omega* **2022**, *7*, 23576–23590. [[CrossRef](#)]
3. Wojciechowska, P.; Cierpiszewski, R. Gelatin—Siloxane Hybrid Monoliths as Novel Heavy Metal Adsorbents. *Appl. Sci.* **2022**, *12*, 1258. [[CrossRef](#)]
4. Didó, C.A.; Coelho, F.L.; Closs, M.B.; Deon, M.; Horowitz, F.; Bernardi, F.; Schneider, P.H.; Benvenuti, E. V Strategy to isolate ionic gold sites on silica surface: Increasing their efficiency as catalyst for the formation of 1,3-diynes. *Appl. Catal. A Gen.* **2020**, *594*, 117444. [[CrossRef](#)]
5. Estevez, R.; Luna, D.; Bautista, F.M. Sulfonated organosilica-aluminum phosphates as useful catalysts for acid-catalyzed reactions: Insights into the effect of synthesis parameters on the final catalyst. *Catal. Today* **2022**, 390–391, 12–21. [[CrossRef](#)]
6. Liu, M.; Wang, L.; Zhang, L.; Zhao, Y.; Chen, K.; Li, Y. In-Situ Silica Xerogel Assisted Facile Synthesis of Fe-N-C Catalysts with Dense Fe-N<sub>x</sub> Active Sites for Efficient Oxygen Reduction. *Small* **2022**, *18*, 202104934. [[CrossRef](#)]
7. Song, L.; Jia, Y.; Jin, X.; Wang, X.; Chen, M.; Wu, Y. Novel hybrid xerogel with CaF<sub>2</sub>:Tb<sup>3+</sup> nanoparticles covalently embedded into silicon-oxygen network through sol-gel process. *J. Lumin.* **2022**, *250*, 119071. [[CrossRef](#)]
8. Vilela, R.R.C.; Zanon, K.P.S.; de Oliveira, M.; de Vicente, F.S.; de Camargo, A.S.S. Structural and photophysical characterization of highly luminescent organosilicate xerogel doped with Ir(III) complex. *J. Sol-Gel Sci. Technol.* **2022**, *102*, 236–248. [[CrossRef](#)]
9. Santos, J.F.M.; Zanuto, V.S.; Ventura, M.; Bramorski, C.B.; Catunda, T. Quantum yield measurements by thermal lens in highly absorbing samples: The case of highly doped rhodamine B organic/silica xerogels. *Phys. Rev. Mater.* **2019**, *3*, 115201. [[CrossRef](#)]
10. Alcantara-garcia, A.; Garcia-casas, A.; Jimenez-morales, A. The effect of the organosilane content on the barrier features of sol-gel anticorrosive coatings applied on carbon steel. *Prog. Org. Coat.* **2020**, *139*, 105418. [[CrossRef](#)]
11. Scotland, K.M.; Shetranjiwalla, S.; Vreugdenhil, A.J. Curable hybrid materials for corrosion protection of steel: Development and application of UV-cured 3-methacryloxypropyltrimethoxysilane-derived coating. *J. Coat. Technol. Res.* **2020**, *17*, 977–989. [[CrossRef](#)]
12. Rodič, P.; Milošev, I.; Lekka, M.; Andreatta, F.; Fedrizzi, L. Corrosion behaviour and chemical stability of transparent hybrid sol-gel coatings deposited on aluminium in acidic and alkaline solutions. *Prog. Org. Coat.* **2018**, *124*, 286–295. [[CrossRef](#)]
13. Hao, S.; Hu, C.; Lin, X. Resistance to Growth of Molds for Wood Modified with Hydrophobic Hybrid Silica Gel Containing Copper Amine Complexes. *Materials* **2021**, *14*, 577. [[CrossRef](#)] [[PubMed](#)]
14. Wang, H.; Yue, W.; Zhang, S.; Zhang, Y.; Li, C.; Su, W. Modification of Silica Xerogels with Polydopamine for Lipase B from *Candida antarctica* Immobilization. *Catalysts* **2021**, *11*, 1463. [[CrossRef](#)]
15. Hatano, K.; Teraki, M.; Nakajima, D.; Yamatsu, T. Controlled release of molasses melanoidin-like product from hybrid organic-inorganic silica xerogels and its application to the phytoextraction of lead through the Indian mustard. *Environ. Sci. Pollut. Res.* **2021**, *28*, 37562–37569. [[CrossRef](#)] [[PubMed](#)]
16. Pérez-Moreno, A.; Reyes-Peces, M.V.; Vilches-Pérez, J.I.; Fernández-Montesinos, R.; Pinaglia-Tobaruela, G.; Salido, M.; de la Rosa-Fox, N.; Piñero, M. Effect of Washing Treatment on the Textural Properties and Bioactivity of Silica/Chitosan/TCP Xerogels for Bone Regeneration. *Int. J. Mol. Sci.* **2021**, *22*, 8321. [[CrossRef](#)] [[PubMed](#)]
17. Kapusuz, D. Sol-gel derived silica/polyethylene glycol hybrids as potential oligonucleotide vectors. *J. Mater. Res.* **2019**, *34*, 3787–3797. [[CrossRef](#)]
18. Goel, H.; Santhiya, D. Effect of pH on bio-inspired synthesis of L-Lysine templated bioactive glass hybrid xerogels for tailored textural and rheological properties. *Mater. Chem. Phys.* **2022**, *281*, 125828. [[CrossRef](#)]
19. Wendels, S.; de Souza Porto, D.; Avérous, L. Synthesis of biobased and hybrid polyurethane xerogels from bacterial polyester for potential biomedical applications. *Polymers* **2021**, *13*, 4256. [[CrossRef](#)]
20. Judeinstein, P.; Sanchez, C. Hybrid organic-inorganic materials: A land of multidisciplinary. *J. Mater. Chem.* **1996**, *6*, 511–525. [[CrossRef](#)]



21. Kaya, G.G.; Deveci, H. Synergistic effects of silica aerogels/xerogels on properties of polymer composites: A review. *J. Ind. Eng. Chem.* **2020**, *89*, 13–27. [[CrossRef](#)]
22. Kolle, J.M.; Sayari, A. Dry gel grafting of mesoporous silica: Application to amine-based CO<sub>2</sub> adsorbents. *Microporous Mesoporous Mater.* **2022**, *343*, 112195. [[CrossRef](#)]
23. Jahandar, M.; Ziaei-azad, H.; Sayari, A. Unprecedented improvement of the hydrothermal stability of amine-grafted MCM-41 silica for CO<sub>2</sub> capture via aluminum incorporation. *Chem. Eng. J.* **2022**, *450*, 138393. [[CrossRef](#)]
24. Yan, J.; Kuang, M.; Zhu, Y.; Chen, Y.; Zhang, C.; Ma, H.; Zhang, X.; Kong, L. Facile, tunable, and environmental friendly synthesis of silica/resorcinol–formaldehyde hybrid xerogels with ultra-low shrinkage using a cationic polyelectrolyte as a soft template. *J. Porous Mater.* **2022**. [[CrossRef](#)]
25. Flores-López, S.L.; Villanueva, S.F.; Rey-Raap, N.; Arenillas, A. Hybrid rf-si xerogels: A cost-effective proposal for insulator materials. *Materials* **2022**, *15*, 265. [[CrossRef](#)] [[PubMed](#)]
26. Ramezani, M.; Vaezi, M.R.; Kazemzadeh, A. The influence of the hydrophobic agent, catalyst, solvent and water content on the wetting properties of the silica films prepared by one-step sol-gel method. *Appl. Surf. Sci.* **2015**, *326*, 99–106. [[CrossRef](#)]
27. Dudás, Z.; Len, A.; Ianăși, C.; Paladini, G. Structural modifications caused by the increasing MTES amount in hybrid MTES/TEOS-based silica xerogels. *Mater. Charact.* **2020**, *167*, 33–36. [[CrossRef](#)]
28. Mageste, R.L.; Sampaio, D.; Mayrink, T.F.; Ahmed, H.; Palhares, H.G.; Nunes, E.H.M.; Houmard, M. Influence of the alcoholic solvent and gelation temperature on the structural and water vapor adsorption properties of silica adsorbents synthesized by sol-gel method without catalyst. *Microporous Mesoporous Mater.* **2022**, *342*, 112114. [[CrossRef](#)]
29. Innocenzi, P. *The Sol-Gel Transition*, 2nd ed.; Springer: Sassari, Italy, 2019; ISBN 978-3-030-20029-9.
30. Zhao, X.; Wang, Y.; Luo, J.; Wang, P.; Xiao, P.; Jiang, B. The Influence of Water Content on the Growth of the Hybrid-Silica Particles by Sol-Gel Method. *Silicon* **2020**, *13*, 3413–3421. [[CrossRef](#)]
31. Estella, J.; Echeverría, J.C.; Laguna, M.; Garrido, J.J. Silica xerogels of tailored porosity as support matrix for optical chemical sensors. Simultaneous effect of pH, ethanol:TEOS and water:TEOS molar ratios, and synthesis temperature on gelation time, and textural and structural properties. *J. Non-Cryst. Solids* **2007**, *353*, 286–294. [[CrossRef](#)]
32. Musgo, J.; Echeverría, J.C.; Estella, J.; Laguna, M.; Garrido, J.J. Ammonia-catalyzed silica xerogels: Simultaneous effects of pH, synthesis temperature, and ethanol:TEOS and water:TEOS molar ratios on textural and structural properties. *Microporous Mesoporous Mater.* **2009**, *118*, 280–287. [[CrossRef](#)]
33. Echeverría, J.C.; Estella, J.; Barbería, V.; Musgo, J.; Garrido, J.J. Synthesis and characterization of ultramicroporous silica xerogels. *J. Non-Cryst. Solids* **2010**, *356*, 378–382. [[CrossRef](#)]
34. Echeverría, J.C.; Moriones, P.; Arzamendi, G.; Garrido, J.J.; Gil, M.J.; Cornejo, A.; Martínez-Merino, V. Kinetics of the acid-catalyzed hydrolysis of tetraethoxysilane (TEOS) by <sup>29</sup>Si NMR spectroscopy and mathematical modeling. *J. Sol-Gel Sci. Technol.* **2018**, *86*, 316–328. [[CrossRef](#)]
35. Rios, X.; Moriones, P.; Echeverría, J.C.; Luquín, A.; Laguna, M.; Garrido, J.J. Characterisation of hybrid xerogels synthesised in acid media using methyltriethoxysilane (MTEOS) and tetraethoxysilane (TEOS) as precursors. *Adsorption* **2011**, *17*, 583–593. [[CrossRef](#)]
36. Moriones, P.; Echeverría, J.C.; Garrido, J.B.P.J. Phenyl siloxane hybrid xerogels: Structure and porous texture. *Adsorption* **2020**, *26*, 177–188. [[CrossRef](#)]
37. Cruz-Quesada, G.; Espinal-Viguri, M.; López-Ramón, M.; Garrido, J. Novel Organochlorinated Xerogels: From Microporous Materials to Ordered Domains. *Polymers* **2021**, *13*, 1415. [[CrossRef](#)]
38. Rios, X.; Moriones, P.; Echeverría, J.C.; Luquín, A.; Laguna, M.; Garrido, J.J. Ethyl group as matrix modifier and inducer of ordered domains in hybrid xerogels synthesised in acidic media using ethyltriethoxysilane (ETEOS) and tetraethoxysilane (TEOS) as precursors. *Mater. Chem. Phys.* **2013**, *141*, 166–174. [[CrossRef](#)]
39. Ospino, I.; Luquín, A.; Jiménez-Ruiz, M.; Pérez-Landazábal, J.I.; Recarte, V.; Echeverría, J.C.; Laguna, M.; Urtasun, A.A.; Garrido, J.J. Computational Modeling and Inelastic Neutron Scattering Contributions to the Study of Methyl-silica Xerogels: A Combined Theoretical and Experimental Analysis. *J. Phys. Chem. C* **2017**, *121*, 22836–22845. [[CrossRef](#)]
40. Cruz-Quesada, G.; Espinal-Viguri, M.; López-Ramón, M.; Garrido, J. Hybrid Xerogels: Study of the Sol-Gel Process and Local Structure by Vibrational Spectroscopy. *Polymers* **2021**, *13*, 2082. [[CrossRef](#)]
41. Estella, J.; De Vicente, P.; Echeverría, J.C.; Garrido, J.J. A fibre-optic humidity sensor based on a porous silica xerogel film as the sensing element. *Sens. Actuators B Chem.* **2010**, *149*, 122–128. [[CrossRef](#)]
42. Echeverría, J.C.; Faustini, M.; Garrido, J.J. Effects of the porous texture and surface chemistry of silica xerogels on the sensitivity of fiber-optic sensors toward VOCs. *Sens. Actuators B Chem.* **2016**, *222*, 1166–1174. [[CrossRef](#)]
43. Echeverría, J.C.; Calleja, I.; Moriones, P.; Garrido, J.J. Fiber optic sensors based on hybrid phenyl-silica xerogel films to detect n-hexane: Determination of the isosteric enthalpy of adsorption. *Beilstein J. Nanotechnol.* **2017**, *8*, 475–484. [[CrossRef](#)]
44. Fidalgo, A.; Ciriminna, R.; Ilharco, L.M.; Pagliaro, M. Role of the alkyl-alkoxide precursor on the structure and catalytic properties of hybrid sol-gel catalysts. *Chem. Mater.* **2005**, *17*, 6686–6694. [[CrossRef](#)]
45. Fidalgo, A.; Ilharco, L.M. Chemical Tailoring of Porous Silica Xerogels: Local Structure by Vibrational Spectroscopy. *Chem. A Eur. J.* **2004**, *10*, 392–398. [[CrossRef](#)] [[PubMed](#)]
46. Innocenzi, P. Infrared spectroscopy of sol-gel derived silica-based films: A spectra-microstructure overview. *J. Non-Cryst. Solids* **2003**, *316*, 309–319. [[CrossRef](#)]

47. Lin, W.; Zheng, J.; Zhuo, J.; Chen, H.; Zhang, X. Characterization of sol-gel ORMOSIL antireflective coatings from phenyltriethoxysilane and tetraethoxysilane: Microstructure control and application. *Surf. Coat. Technol.* **2018**, *345*, 177–182. [CrossRef]
48. Launer, P.J.; Arkles, B. Infrared Analysis of Organosilicon Compounds. In *Silicon Compd. Silanes Silicones*, 3rd ed.; Arkles, B., Larson, G.L., Eds.; Gelest, Inc.: Morrisville, PA, USA, 2013; pp. 175–178. ISBN 978-0-578-12235-9.
49. Park, E.S.; Ro, H.W.; Nguyen, C.V.; Jaffe, R.L.; Yoon, D.Y. Infrared spectroscopy study of microstructures of poly(silsesquioxane)s. *Chem. Mater.* **2008**, *20*, 1548–1554. [CrossRef]
50. Guo, M.; Kanezashi, M.; Nagasawa, H.; Yu, L.; Yamamoto, K.; Gunji, T.; Ohshita, J.; Tsuru, T. Tailoring the microstructure and permeation properties of bridged organosilica membranes via control of the bond angles. *J. Memb. Sci.* **2019**, *584*, 56–65. [CrossRef]
51. Hayami, R.; Ideno, Y.; Sato, Y.; Tsukagoshi, H.; Yamamoto, K.; Gunji, T. Soluble ethane-bridged silsesquioxane polymer by hydrolysis–condensation of bis(trimethoxysilyl)ethane: Characterization and mixing in organic polymers. *J. Polym. Res.* **2020**, *27*, 316. [CrossRef]
52. Marchesi, S.; Carniato, F.; Palin, L.; Boccaleri, E. POSS as building-blocks for the preparation of polysilsesquioxanes through an innovative synthetic approach. *Dalt. Trans.* **2015**, *44*, 2042–2046. [CrossRef]
53. Choi, S.S.; Lee, A.S.; Lee, H.S.; Baek, K.Y.; Choi, D.H.; Hwang, S.S. Synthesis and characterization of ladder-like structured polysilsesquioxane with carbazole group. *Macromol. Res.* **2011**, *19*, 261–265. [CrossRef]
54. Wu, J.; Mather, P.T. POSS polymers: Physical properties and biomaterials applications. *Polym. Rev.* **2009**, *49*, 25–63. [CrossRef]
55. Choi, S.S.; Lee, A.S.; Hwang, S.S.; Baek, K.Y. Structural Control of Fully Condensed Polysilsesquioxanes: Ladder-like vs Cage Structured Polyphenylsilsesquioxanes. *Macromolecules* **2015**, *48*, 6063–6070. [CrossRef]
56. Jung, J.; Won, J.; Hwang, S.S. Highly selective composite membranes using ladder-like structured polysilsesquioxane for a non-aqueous redox flow battery. *J. Memb. Sci.* **2020**, *595*, 117520. [CrossRef]
57. Depla, A.; Verheyen, E.; Veyfeyken, A.; Van Houteghem, M.; Houthoofd, K.; Van Speybroeck, V.; Waroquier, M.; Kirschhock, C.E.A.; Martens, J.A. UV-Raman and <sup>29</sup>Si NMR spectroscopy investigation of the nature of silicate oligomers formed by acid catalyzed hydrolysis and polycondensation of tetramethylorthosilicate. *J. Phys. Chem. C* **2011**, *115*, 11077–11088. [CrossRef]
58. Handke, M.; Jastrzębski, W. Vibrational spectroscopy of the ring structures in silicates and siloxanes. *J. Mol. Struct.* **2004**, *704*, 63–69. [CrossRef]
59. Hagiwara, Y.; Shimojima, A.; Kuroda, K. Alkoxysilylated-Derivatives of Double-Four-Ring Silicate as Novel Building Blocks of Silica-Based Materials. *Chem. Mater.* **2008**, *20*, 1147–1153. [CrossRef]
60. Nowacka, M.; Kowalewska, A.; Makowski, T. Structural studies on ladder phenylsilsesquioxane oligomers formed by polycondensation of cyclotetrasiloxanetetraols. *Polymer* **2016**, *87*, 81–89. [CrossRef]
61. Blanco, I.; Bottino, F.A.; Abate, L. Influence of n-alkyl substituents on the thermal behaviour of Polyhedral Oligomeric Silsesquioxanes (POSSs) with different cage's periphery. *Thermochim. Acta* **2016**, *623*, 50–57. [CrossRef]
62. Vasil'ev, S.G.; Volkov, V.I.; Tatarinova, E.A.; Muzafarov, A.M. A Solid-State NMR Investigation of MQ Silicone Copolymers. *Appl. Magn. Reson.* **2013**, *44*, 1015–1025. [CrossRef]
63. Uhlig, F.; Marsman, H.C. <sup>29</sup>Si NMR—Some Practical Aspects. *Silicon Compd. Silanes Silicones A Surv. Prop. Chem.* **2008**, *2*, 208–222.
64. Cheng, X.; Chen, D.; Liu, Y. Mechanisms of silicon alkoxide hydrolysis-oligomerization reactions: A DFT investigation. *ChemPhysChem* **2012**, *13*, 2392–2404. [CrossRef]
65. Pierre, A.C. *Introduction to Sol-Gel Processing*; Springer Nature: Berlin, Germany, 2020; ISBN 9780792381211.
66. Laird, M.C.; Yokoyama, J.; Carcel, C.; Unno, M.; Bartlett, J.R.; Wong Chi Man, M. Sol-gel processing of polyhedral oligomeric silsesquioxanes: Nanohybrid materials incorporating T<sub>8</sub> and T<sub>10</sub> cages. *J. Sol-Gel Sci. Technol.* **2020**, *95*, 760–770. [CrossRef]
67. Wu, X.; Qin, Z.; Zhang, W.; Yang, R. KCl nanoparticles-loaded octaphenylsilsesquioxane as an efficient flame retardant for polycarbonate. *React. Funct. Polym.* **2022**, *177*, 105284. [CrossRef]
68. Kamiya, K.; Dohkai, T.; Wada, M.; Hashimoto, T.; Matsuoka, J.; Nasu, H. X-ray diffraction of silica gels made by sol-gel method under different conditions. *J. Non-Cryst. Solids* **1998**, *240*, 202–211. [CrossRef]
69. Jo, Y.Y.; Lee, A.S.; Baek, K.Y.; Lee, H.; Hwang, S.S. Multi-crosslinkable self-healing polysilsesquioxanes for the smart recovery of anti-scratch properties. *Polymer* **2017**, *124*, 78–87. [CrossRef]
70. Garrido, J.; Linares-solano, A.; Martín-Martínez, J.M.; Molina-Sabio, M.; Rodríguez-Reinoso, F.; Torregrosa, R. Use of N<sub>2</sub> vs: CO<sub>2</sub> in the Characterization of Activated Carbons. *Langmuir* **1987**, *3*, 76–81. [CrossRef]
71. Thommes, M.; Kaneko, K.; Neimark, A.V.; Olivier, J.P.; Rodríguez-Reinoso, F.; Rouquerol, J.; Sing, K.S.W. Physisorption of gases, with special reference to the evaluation of surface area and pore size distribution (IUPAC Technical Report). *Pure Appl. Chem.* **2015**, *87*, 1051–1069. [CrossRef]
72. Kowalewska, A.; Fortuniak, W.; Handke, B. New hybrid silsesquioxane materials with sterically hindered carbosilane side groups. *J. Organomet. Chem.* **2009**, *694*, 1345–1353. [CrossRef]
73. Moriones, P. *Síntesis y Caracterización de Xerogeles Silíceos Híbridos (RTEOS/TEOS; R = P, Ph)*; Universidad Pública de Navarra: Pamplona, Spain, 2015; Available online: <https://academica-e.unavarra.es/handle/2454/20351> (accessed on 13 October 2022).
74. Kickelbick, G. *Hybrid Materials Synthesis, Characterization, and Applications*; John Wiley & Sons: New York, NY, USA, 2007; ISBN 9783527312993.
75. Torres-Luna, J.A.; Carriazo, J.G. Porous aluminosilicic solids obtained by thermal-acid modification of a commercial kaolinite-type natural clay. *Solid State Sci.* **2019**, *88*, 29–35. [CrossRef]

76. Sakka, S. *Handbook of Sol-Gel Science and Technology: Processing, Characterization and Applications. Volume II: Characterization of Sol-Gel Materials and Products*, 1st ed.; Sakka, S., Almeida, R.M., Eds.; Kluwer Academic Publishers: Osaka, Japan, 2005; ISBN 1-4020-7967-2.
77. Rouquerol, J.; Llewellyn, P.; Rouquerol, F. Is the BET equation applicable to microporous adsorbents? *Stud. Surf. Sci. Catal.* **2007**, *160*, 49–56. [[CrossRef](#)]
78. Rouquerol, F.; Rouquerol, J.; Sing, K.S.W.; Llewellyn, P.; Maurin, G. *Adsorption by Powders and Porous Solids Principles, Methodology and Applications*, 2nd ed.; Academic Press: San Diego, CA, USA, 1999; ISBN 978-0-12-598920-6.
79. García-Martínez, J.; Cazorla-Amorós, D.; Linares-Solano, A. Further evidences of the usefulness of CO<sub>2</sub> adsorption to characterise microporous solids. *Stud. Surf. Sci. Catal.* **2000**, *128*, 485–494. [[CrossRef](#)]